

Metadata of the chapter that will be visualized in SpringerLink

Book Title	Clinical and Biomedical Engineering in the Human Nose	
Series Title		
Chapter Title	Clinical CFD Applications 2	
Copyright Year	2021	
Copyright HolderName	Springer Nature Singapore Pte Ltd.	
Corresponding Author	Family Name	Yu
	Particle	
	Given Name	Feng
	Prefix	
	Suffix	
	Role	
	Division	
	Organization	Oklahoma State University
	Address	Stillwater, USA
	Email	yu.feng@okstate.edu
Author	Family Name	Hamideh
	Particle	
	Given Name	Hayati
	Prefix	
	Suffix	
	Role	
	Division	
	Organization	Oklahoma State University
	Address	Stillwater, USA
	Email	
Author	Family Name	Alister
	Particle	
	Given Name	Bates
	Prefix	
	Suffix	
	Role	
	Division	
	Organization	Cincinnati Children's Hospital
	Address	Cincinnati, USA
	Email	
Author	Family Name	Walter
	Particle	
	Given Name	Koch
	Prefix	
	Suffix	

	Role	
	Division	
	Organization	AIT Angewandte Informationstechnik Forschungsgesellschaft mbH
	Address	Graz, Austria
	Email	
Author	Family Name	Matthias
	Particle	
	Given Name	Lehner
	Prefix	
	Suffix	
	Role	
	Division	
	Organization	AIT Angewandte Informationstechnik Forschungsgesellschaft mbH
	Address	Graz, Austria
	Email	
Author	Family Name	Odo
	Particle	
	Given Name	Benda
	Prefix	
	Suffix	
	Role	
	Division	
	Organization	AIT Angewandte Informationstechnik Forschungsgesellschaft mbH
	Address	Graz, Austria
	Email	
Author	Family Name	Ramiro
	Particle	
	Given Name	Ortiz
	Prefix	
	Suffix	
	Role	
	Division	
	Organization	AIT Angewandte Informationstechnik Forschungsgesellschaft mbH
	Address	Graz, Austria
	Email	
Author	Family Name	Gerda
	Particle	
	Given Name	Koch
	Prefix	
	Suffix	
	Role	
	Division	
	Organization	AIT Angewandte Informationstechnik Forschungsgesellschaft mbH
	Address	Graz, Austria
	Email	

Abstract

This chapter is the second of the two chapters demonstrating the wide variety of CFD studies in clinical applications presented from leading researchers in their respective fields. This chapter covers the latest research techniques and outcomes in whole lung modelling; Modeling the Effect of Airway Motion Using Dynamic Imaging; and Automatic reconstruction of the nasal geometry from CT scans.

Chapter 10

Clinical CFD Applications 2



Feng Yu, Hayati Hamideh, Bates Alister, Koch Walter, Lehner Matthias,
Benda Odo, Ortiz Ramiro, and Koch Gerda

Abstract This chapter is the second of the two chapters demonstrating the wide variety of CFD studies in clinical applications presented from leading researchers in their respective fields. This chapter covers the latest research techniques and outcomes in whole lung modelling; Modeling the Effect of Airway Motion Using Dynamic Imaging; and Automatic reconstruction of the nasal geometry from CT scans.

10.1 Whole-Lung Modelling

Yu Feng, Hamideh Hayati

10.1.1 Introduction

To accurately evaluate the lung dose of inhaled particulate matters from the nose, the influence of lower respiratory tract on the upstream airflow patterns in human nose needs to be modeled. Specifically, the presence of lower respiratory tract will alter the impedance of the expiratory airflows and the resultant particle transport dynamics backflowing into the nasal cavity. Therefore, it is necessary to improve predictive capabilities of computational fluid-particle dynamics (CFPD), i.e., the whole-lung modeling strategy, to precisely estimate the aerosol deposition from nasal cavity to alveoli with full inhalation-exhalation breathing cycles, which is difficult to acquire

F. Yu (✉) · H. Hamideh
Oklahoma State University, Stillwater, USA
e-mail: yu.feng@okstate.edu

B. Alister
Cincinnati Children's Hospital, Cincinnati, USA

K. Walter · L. Matthias · B. Odo · O. Ramiro · K. Gerda
AIT Angewandte Informationstechnik Forschungsgesellschaft mbH, Graz, Austria

© Springer Nature Singapore Pte Ltd. 2021
K. Inthavong et al. (eds.), *Clinical and Biomedical Engineering
in the Human Nose*, Biological and Medical Physics, Biomedical Engineering,
https://doi.org/10.1007/978-981-15-6716-2_10

via in vitro and in vivo methodologies [13, 21, 37]. The overall complexity of the lung with bifurcating architecture, hierarchical cellular composition, and continual dynamic motion results in complex fluid phenomena which perplex deposition of inhaled aerosols.

Whole-lung modeling capabilities are not only able to provide a full map of regional depositions of inhaled aerosols, but also enable the accurate simulation of expiratory particle dynamics after the inhalation. Specifically, simulations using the truncated subject-specific airway geometries reconstructed from CT/MRI data only contain airways up to generation 9 (G9). The missing lower airways force the researchers to make assumptions on how many particles will be able to “re-enter” the flow domain from the truncated airway outlets during the exhalation after the inhalation. With the whole-lung modeling strategies, the lung aerosol dynamics during the full inhalation-exhalation cycles can be predicted without such ad-hoc simplifications. Whole-lung modeling efforts have been made to demonstrate that because of their small size, micro-to-nano scale toxic and/or therapeutic aerosols that vastly exist in the ambient environment are respirable and can penetrate the peripheral lung and enter the systemic region via the air-blood barriers [13, 15, 16, 22, 27, 35–40, 47, 48, 74, 75, 78, 81].

Due to the morphological complexity of the human respiratory system, and the limited resolution of medical imaging techniques [15, 20, 37, 59], identified challenges to develop whole-lung models are: (1) the lack of small-airway CT/MRI data for airway reconstructions [20], and (2) the extremely high computational cost of full-scale CFPD simulations of all airways in entire 23 generations [36, 37]. Accordingly, research efforts have been made to develop alternative whole-lung modeling strategies to optimize the balance between computational accuracy and efficiency [13, 15, 35–40, 47, 48, 74, 75, 78, 81], which are discussed in the next section.

10.1.2 Existing Whole-Lung Modeling Strategies

Realistic airway configurations are currently restricted to the few upper airway generations since lower airway configurations are not easy to reconstruct due to the limited resolution of the scanned images. Moreover, even if the entire lung was fully segmentable, it is not computationally feasible to simulate the full lung tree accurately, because it requires billions of 3D mesh elements [15, 37, 59]. Therefore, several common strategies have been employed in existing whole-lung models: (1) using equivalent geometry (e.g., trumpet) to represent the entire tracheobronchial tree, (2) reducing the degree of freedom (DOF) of the whole lung airway trees by truncating airways and applying advanced coupled boundary conditions [36, 37, 59, 74, 75, 78], and (3) by simplifying small airways using 1D pipelines or 2D in-plane airway models instead of 3D geometries [74, 81].

Specifically, popular approaches for simulating inhaled particle deposition are ‘trumpet’ model [73], deterministic single and multi-path models [1, 13, 48, 54], and stochastic multi-path models [33, 34, 47]. The stochastic model of human lung

consider asymmetry and randomness of the airway system, as well as, variation in parameters (inter-subject variation), i.e., diameter and length of the tubes, branching and gravity angles and the number of bifurcation in each bronchial pathway [34]. In contrast, deterministic approaches do not take the inter-subject variability into account [37].

10.1.2.1 Trumpet Models

The trumpet model [73] is one of the simplified deterministic models that consider the tracheobronchial tree as an axisymmetric trumpet matching the morphometric data of the deterministic Weibel [80] model. Choi and Kim [13] developed a single-path mathematical model, i.e., the two-dimension (2D) trumpet model with connected alveoli [73], to estimate the whole-lung particle deposition. They considered both axial and lateral transport of inhaled particles with the contraction and expansion of alveoli walls. Figure 10.1a demonstrates the 2D trumpet geometry to represent the human lung. Specifically, the alveolar region present G18 to G23. The trumpet is designed based on the fact that the volume of each generation increases from G1 to G23. Although the computational efficiency using the 2D trumpet model is high, the regional deposition results are not predictive, because of the simple inlet conditions and semi-analytical correlations for the deposition mechanisms. Such a 2D trumpet model may not be able to predict lung aerosol dynamics, especially related to the dense particle suspensions from dry powder inhalers (DPIs), in which the interactions between particles may significantly affect particle trajectories in the lung, but cannot be modeled using the 2D trumpet model. Kolanjiyil and Kleinstreuer [37] further developed a 3D trumpet modeling approach, i.e., the whole-lung airway model (WLAM). Considering the fact that the extra-thoracic airway has significant effects on the pulmonary air-flow patterns and the resultant particle transport and deposition, they connected an idealized upper airway model with the 3D trumpet, which can be replaced by subject-specific nasal cavity model (see Fig. 10.1b). By adding an artificial force in the radial directions in the trumpet, WLAM is able to provide reasonably accurate depositions compared to experimental data within the full inhalation-exhalation cycle. The trumpet was divided into multiple regions to represent different airway generations. Specifically, the division is done to equalize the regional volumes to the volumes of certain generations. Furthermore, the lung deformation effect was also approximately achieved by the deformation of the wall at the bottom of the trumpet. However, since the trumpet in WLAM is still axisymmetric, the effect of realistic asymmetric airway features were not able to be captured. Another limitation of the model is that it is only accurate to predict particles larger than 400 nm.

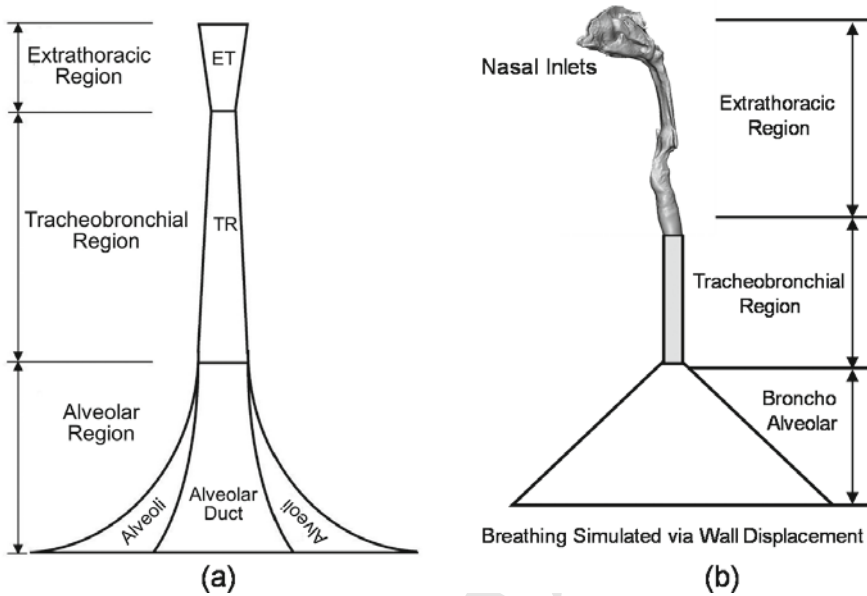


Fig. 10.1 Flow-domain schematics of trumpet models: **a** the 2D trumpet model [13], and **b** the whole-lung airway model [37] (Reprinted from [13, 37], with permission from Taylor and Francis as well as Elsevier)

10.1.2.2 Single-Path and Multi-path Models with Truncations

To simultaneously capture the asymmetrical effect of the airway trees and keep the computational efficiency high, another set of whole-lung modeling strategies is to truncate the branches of the lung geometry and solve the governing equations for one single branch coupling with appropriate boundary conditions at those truncated airways. Modeling the pulmonary routes from mouth/nose to G9 can be achieved by geometry reconstructions using clinical data. However, due to the limitation of medical imaging resolution, small airway reconstructions have been done by connecting idealized bifurcation unit with different geometric dimensions [35, 36, 47, 48, 75, 78]. Specifically, Zhang et al. [81] made the first effort to decompose the complex airway network from the trachea to G17 into a series of detached multiple triple bifurcation units (TBU) [80]. Using an improved modeling strategy based on Zhang et al. [81], Longest et al. [47, 48] developed the stochastic individual paths (SIP) and multiple stochastic individual paths (MSIP) approaches to represent the whole-lung geometry. Compared to the coupling method applied on detached airway geometries [80], this model is able to simulate lung aerosol dynamics with transient inhalation-exhalation breathing cycles.

Also, to model the entire conductive zone, researchers developed a deterministic reduced lung geometry model up to G16 [75, 78]. Figure 10.2 shows the details about

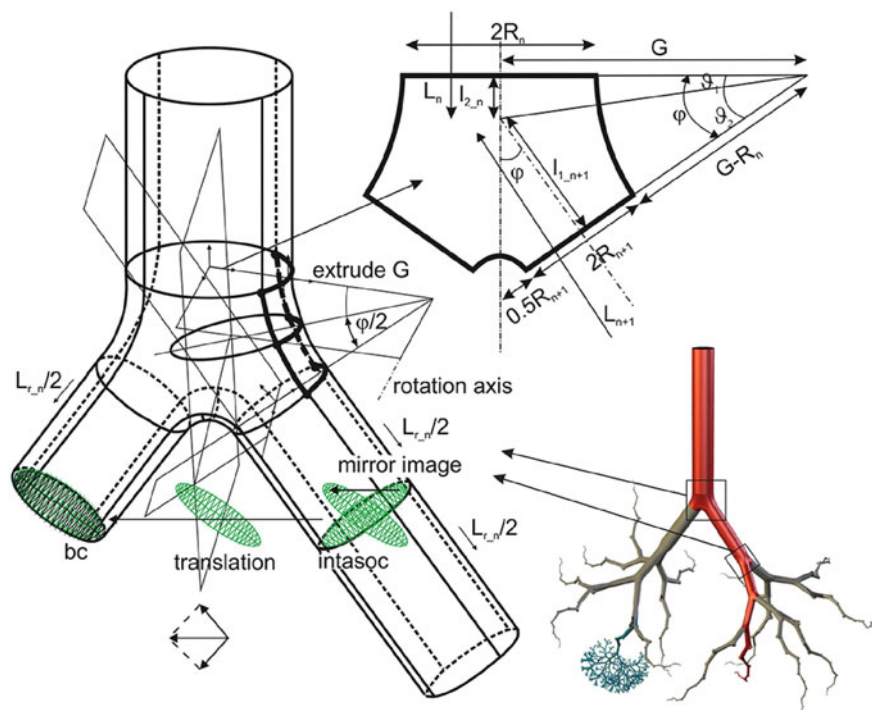


Fig. 10.2 Construction of the reduced lung geometry model (Reprinted from [75], with permission from Wiley)

how the reduced lung geometry model was generated and how the boundary condition was defined at the truncated outlets. Specifically, coupled boundary conditions are applied at the truncated branches, obtained from the complete airway routes. The flow variables were mapped from the resolved pathway to the unresolved truncated branch.

In addition, for the separate effort done for modeling the deep lung and the respiratory zone has been done by Koullapis et al. [40] using an idealized 10-generation bifurcation tree and acini models. The model is shown in Fig. 10.3. This model is capable of tracking the particles that remained suspending during the inhalation phase in the deep lung, and their backflow motion during the exhalation with no assumptions made. However, the disadvantage of this model is lack of realistic randomness of the airway morphology. Indeed, the whole airway tree was constructed by connecting scaled single bifurcations from the same single bifurcation geometry. Therefore, the branching angle and ratios of parent-to-daughter tubes diameter and length-to-diameter are constant for all the generations, which is not physiologically true. The rigid-wall assumption is another disadvantage of the aforementioned model. Furthermore, the acinar model employed in this model represented about 12% of the total acinus, which led to under-estimated acinar deposition of particles, since there are two additional acinar generations in the human lung.

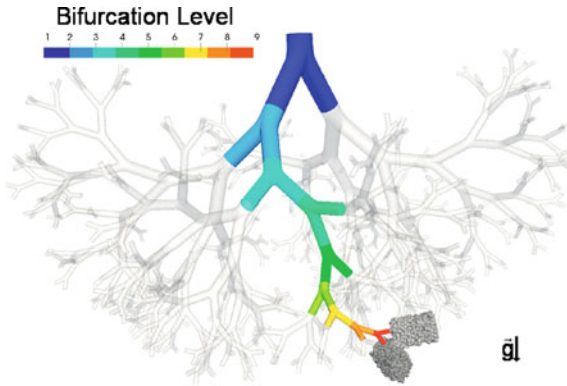


Fig. 10.3 The developed simplified deep lung model (Reprinted from [40], with permission from Elsevier)

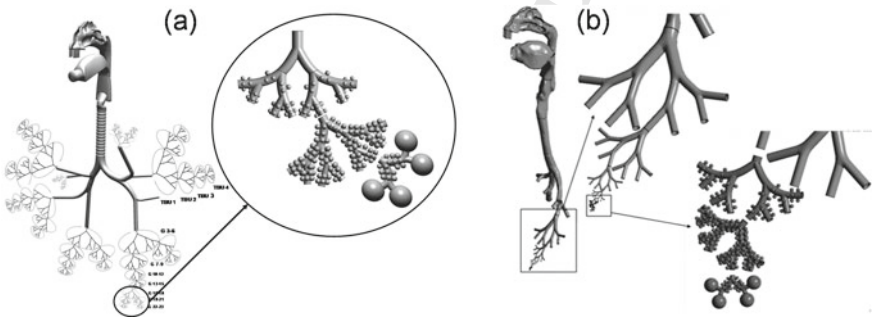


Fig. 10.4 Schematics of (a) the whole-lung model using an idealized human upper air-way model and TBU cascades [36], and (b) the whole-lung dual-path model using an subject-specific human upper airway model and TBU cascades

Moreover, Kolanjiyil and Kleinstreuer [36] combined an idealized upper airway model and a series of TBUs to generate the representative whole-lung model (see Fig. 10.4a). Using the fluid-structure interaction (FSI) approach, this whole-lung model [15] is able to study the effect of alveolar deformations on the pulmonary airflow pattern and the resultant particle dynamics. However, the uniform zero-gauge pressure boundary conditions applied at truncated outlets may introduce errors on pulmonary airflow predictions. In addition, the asymmetrical and non-planar nature of the airway, which influence both fluid flow and particle deposition were not considered. Later, Kolanjiyil and Kleinstreuer [38] built another dual-path whole lung model (see Fig. 10.4b). Instead of using the idealized upper airway geometry, they employed a subject-specific human upper airway model widely used in computational and numerical lung aerosol dynamics research [19, 28, 70, 71].

10.1.2.3 Full 3D-1D Airway-Tree Models Without Truncations

Efforts have been also made to achieve the whole-lung modeling capability with reasonable computational efficiency via reducing the DOF of airways without truncating a portion of the tracheobronchial tree. As the prototype of this type of whole-lung simulation strategy, the impedance model was developed which simplifies the whole lung airway structure using one-dimensional (1D) pipelines [72]. However, due to the existence of strong secondary flows in lateral directions from G1 to G6, the airflow field cannot be captured accurately by solving the 1D governing equation systems. To address such disadvantages, a fully coupled 3D-1D approach was developed based on asymmetric physiological characteristics of the realistic lung airway trees [15, 51, 57, 74, 76]. Specifically, Comerford et al. [15] utilized coupled 3D-1D modeling approach to study pulmonary mechanics of the entire conducting zone under mechanical ventilation. By using this method, the conducting zone of the airway can be modeled efficiently and results in finding important pressure and flow data. In this approach, pressure domain in down-stream (1D) domain obtained from the impedance model used to find the time dependence pressure at the outflow of the 3D domain. To couple 1D model to 3D model, Dirichlet or Neumann boundary conditions were employed [76]. In order to estimate the lung input impedance, Ma and Lutchen [51] applied a model combining 3D CFD simulation in upper and central airway and 1D transmission line-like model for the small airways, which they called hybrid computational model for the human lung. They simulated unsteady flow in upper airway and lower airway up to G6 with impedance (i.e., time-dependent pressure) boundary conditions. The small airways from G6 to alveoli were represented by corresponding small airway trees in the hypothetical airway tree model [74]. Viscoelastic alveoli tissue unit was attached to the end of the conducting zone. The 3D-1D whole-lung models are able to efficiently simulate the pulmonary airway fields in the entire pulmonary system. However, this modeling approach has not been further developed to predict the transport and deposition of inhaled particles.

10.1.3 The Future of Whole-Lung Modeling

For patients with pre-existing lung diseases, including emphysema, asthma, cystic fibrosis (CF), and idiopathic pulmonary fibrosis (IPF), etc., lung dynamic motion, breathing pattern, patient-specific geometries, age, and disease state are all known to contribute to the alteration of airflow and inhaled particle dynamics in the pulmonary system, yet no computational whole-lung models currently incorporates any one of these variables to successfully predict aerosol transport and deposition. Existing whole-lung models are not able to cope with the challenges to:

- Recover the realistic real-time lung deformations considering fluid-structure interaction (FSI);
- Consider soft palate and glottis motions;

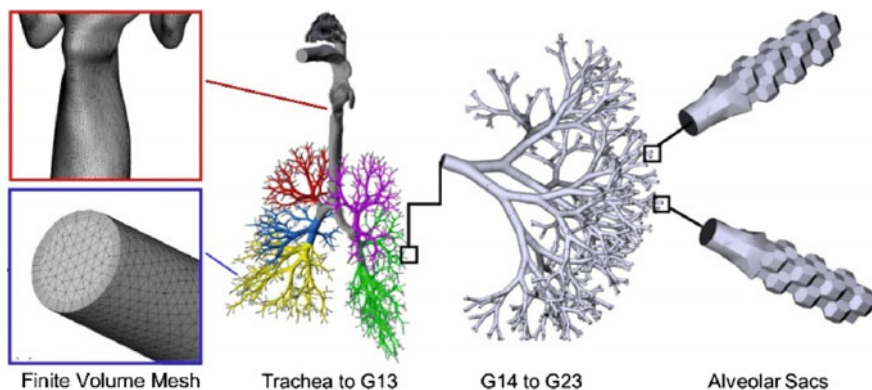


Fig. 10.5 The next-generation 3D elastic whole-lung model covering the entire conducting and respiratory zones

- Capture the disease-specific mucus movement and clearance of inhaled aerosols driven by cilia; and
- Predict the translocation of inhaled drugs or toxicants to clinical endpoints.

Therefore, the multiphase flow phenomena (air-mucus-aerosol transport) in the healthy and diseased human respiratory systems are still not comprehensively modeled and studied. Hence, there is still a gap among the whole-lung modeling capabilities, to sufficiently investigate how pre-existing lung disease including lung morphology and stiffness changes affect the advection and diffusion in pulmonary airways, the mucus movement and clearance, and the resultant variations of the inhaled therapeutic drug delivery efficiency. Thus, the future work to build the next-generation whole-lung model is to enable the development of personalized aerosol therapeutics optimized for patient-specific variables including patient age, anatomy, breathing maneuvers, and pathophysiology. The next-generation whole-lung model should be able to answer the fundamental question of biological fluid dynamics on how the physiological and biomechanical feature variations between the healthy and diseased airways will affect pulmonary airflow dynamics, mucus movement, and the advection and diffusion of tracing particles/gases into small airways. The next-generation of whole-lung model, i.e., “living lung model”, should provide a scientific basis for further understanding altered characteristics of diseased airways and their implications to clinical diagnosis and treatment as well as evaluation of drug delivery. The most straightforward methodology is to integrate the elastic lung model [76] into the modeling ideas for conducting and respiratory zones [40, 75], to form the prototype of the next-generation of virtual whole-lung model (see Fig. 10.5).

10.2 Modeling the Effect of Airway Motion Using Dynamic Imaging

Bates, Alister

10.2.1 Introduction and Clinical Significance

Many airway diseases involve abnormal motion of the airway wall. This motion may result in the airway lumen narrowing or entirely collapsing, either of which will affect the patient's ability to breathe. Abnormal airway motion may occur in various portions of the airway. Examples include obstructive sleep apnea (OSA), a condition in which the upper airway collapses during sleep, often because the soft palate and/or tongue collapse against the posterior wall of the pharynx. Vocal cord dysfunction occurs when the vocal cords close abnormally during breathing. The larynx, trachea, and bronchi collapse in laryngomalacia, tracheomalacia, and bronchomalacia, respectively. Even in otherwise healthy subjects, the nasal valve can collapse during rapid inhalation.

Airway motion occurs for a variety of reasons. Firstly, the air pressure within the airway varies throughout the breathing cycle from below atmospheric pressure during inhalation to above atmospheric pressure during exhalation. These pressure forces act on the airway walls and can cause them to collapse inwards under low pressures or expand outwards under high pressure.

Secondly, the airway below the thoracic inlet (approximately one third of the way down the trachea) is within the thoracic cavity. Therefore, the intrathoracic pressures generated by the diaphragm and intercostal muscles to expand and contract the lungs also act on the exterior of the intrathoracic airway walls. This effect leads to conditions such as tracheomalacia, in which the intrathoracic pressure generated to exhale air from the lungs is enough to collapse the trachea. The trachea may collapse if the cartilaginous tissues that provide its structure are abnormally soft and are unable to support the membrane in the posterior tracheal wall, the trachealis. However, a healthy trachea may also collapse if the intrathoracic pressure becomes unusually high, due to respiratory demands or lung parenchyma abnormalities. In this latter case, the condition is known as excessive dynamic airway collapse (EDAC).

The third mechanism for airway motion is neuromuscular control of the structures surrounding the airway, many of which are muscular, such as the tongue, soft palate, and pharyngeal walls. Opening the jaw or changing head position also alter the airway shape and size. Patients control these structures in order to maintain airway patency, but their ability to do so depends on their anatomy, ability to sense airflow, muscle tone, and the pressure forces they are working against. This factor also varies according to the subject's level of arousal, leading to sleep related conditions such as OSA.

Regardless of the location or cause of airway collapse, dynamic narrowing will increase the amount of energy required to respire, which is known as the work of breathing. The airway resistance will also increase during the portion of the breath in which the airway is narrowed, thereby increasing the pressure difference between the lungs and atmospheric pressure or limiting peak flow rates. This effect may, in turn, alter the patient's respiratory flow waveform. Clinically, the important question is whether airway motion affects the patient's symptoms or wellbeing due to increased airway resistance and/or work of breathing. CFD simulations have the potential to quantify these factors but require realistic airway motion to be incorporated as a boundary condition.

Two approaches have been used for modelling airway motion. The first is fluid structure interaction (FSI). These models simulate both the airflow and the structures surrounding the airway by modeling structural deformations using material properties such as Young's Modulus. They have been employed to model passive motion of the airway (i.e. when the airway moves solely due to air pressure in the lumen) [2, 62, 79, 82–84]. However, tissue properties may be difficult to calculate in vivo and vary significantly across the tissues surrounding the upper airway and between subjects with various pathological conditions [12]. Furthermore, neuromuscular control of structures surrounding the airway is difficult to predict and incorporate into FSI models. The tissues may move out-of-phase with the breath profile, or may move differently from breath to breath [58, 68]. Therefore, a second technique has been implemented to model conditions where neuromuscular control of the airway plays a significant role in airway motion, such as OSA. In this technique the in vivo motion of the airway is extracted from cine imaging and applied to the surface of the CFD model, causing the modeled airway surface to move as the real airway moves in vivo. This technique will be described in more detail below.

10.2.2 3D Cine Imaging

Three-dimensional, time varying CFD simulations require information on the airway motion in all directions and across the airway surface throughout the period of interest. This information can be obtained from four-dimensional (4D—time and three spatial dimensions) cine image volumes acquired from either computed tomography (CT) or magnetic resonance imaging (MRI). CT has the advantage over MRI of a higher contrast to noise ratio and is therefore easier to determine the position of the airway at each time-point in a cine image sequence. CT also allows for high spatial resolution (approximately $0.4 \times 0.4 \times 0.4$ mm) which yields accurate reconstruction of the airway shape and motion, and lower dynamic times (i.e. the amount of time between one image and the next in the sequence—as low as 135 ms, which is half the gantry rotation time), making it more suitable for fast moving structures. An example of airway motion captured with CT is shown in Fig. 10.6a. However, the disadvantage of this modality is that CT imaging exposes subjects to ionizing radiation [61].

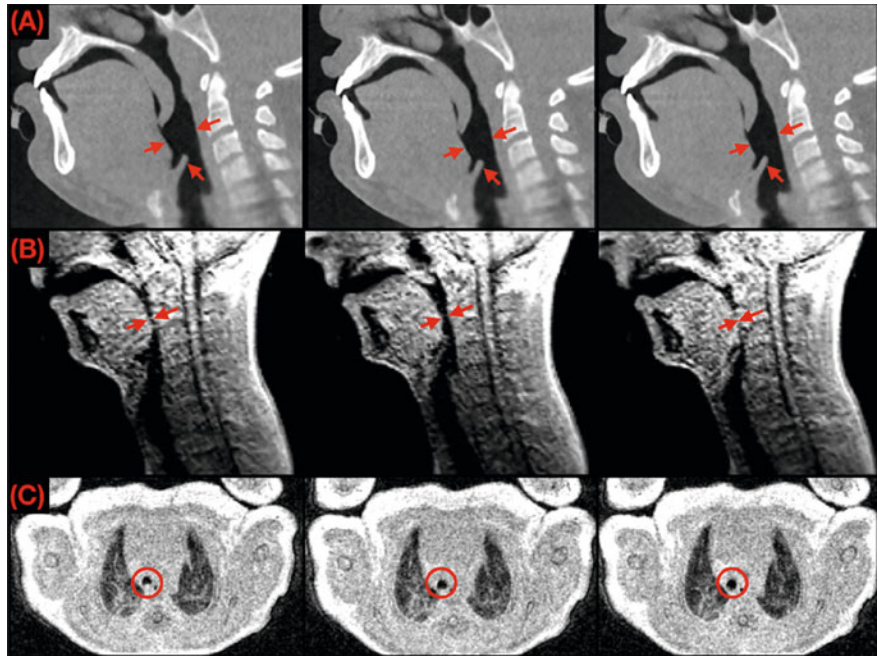


Fig. 10.6 **a** A sagittal slice through the upper airway of an 18-year-old patient with OSA taken from a 4D dynamic CT image. The slice is shown at three instants through a breath. There is a subtle change in caliber of the retroglottal airway and the epiglottis moves anteriorly (red arrows). **b** A sagittal slice through the upper airway of an 11-year-old patient with OSA at three instants taken from real-time cine MRI. The retroglottal airway caliber starts narrow (left image, red arrows), widens (central image), and then collapses completely (right image). **c** An axial slice showing the intrathoracic trachea in a neonatal patient with tracheomalacia at three instants. In the first image (left), the rear wall of the trachea has collapsed inwards creating a “D” shaped lumen (red circle). In the central image, the rear wall has started to move posteriorly, and it keeps moving until the trachea is almost circular (right image)

An alternative modality is MRI, which does not employ ionizing radiation and therefore can be used in vulnerable populations, such as children, and in serial studies in which patients are imaged before and after treatment or to assess disease progression. Patients may also be imaged for long periods in order to capture particular events, such as airway collapse in OSA, which may only occur a few times per hour. MRI provides two techniques for achieving three-dimensional imaging of dynamic anatomy. The first is real-time cine imaging. Fast cine MRI techniques, such as enhanced T1 high-resolution isotropic volume excitation (THRIVE), can produce 3D images of the airway every 300 ms, with spatial resolution of $2.0 \times 2.0 \times 3.0$ mm [8]. This temporal resolution is not high enough to capture fine details of the airway motion, such as oscillations of the uvula due to snoring, but does capture coarse airway motion. The value of this technique is the high temporal resolution and real-time capture of events that do not occur every breath. Figure 10.6b shows real-time MRI of complete collapse of the retroglottal airway in a patient with OSA.

The second MRI approach for three-dimensional imaging of dynamic anatomy utilizes retrospective gating of the raw MRI data, which is modulated by respiratory motion due to imaging physics. High-resolution imaging data is continually obtained for several minutes while the subject performs tidal breathing. The data is then sorted into bins depending on when in the respiratory cycle it was captured. Images are reconstructed from each bin of data, providing average images of the typical airway shape during that portion of the breath over the imaging period [29]–[17]. For example, data could be sorted into inspiratory and expiratory bins or into many shorter periods throughout the respiratory cycle. Using more bins increases the temporal resolution of the resultant images at the expense of the images' signal to noise ratio [25]. The advantage of this method over real time cine MRI is that higher spatial resolution images are obtained (a CT-like submillimeter resolution, such as $0.7 \times 0.7 \times 0.7$ mm) and higher temporal resolution (e.g. 90 ms) is possible depending on the required signal to noise ration and imaging duration. The disadvantage is that the images represent averages of the airway shape during particular periods of the breathing cycle rather than the instantaneous “snap shots” provided by real-time cine MRI. This renders the technique suitable for rhythmic airway motion such as tracheal collapse in patients with tracheomalacia, but unsuitable for the occasional upper airway collapses in patients with OSA. An example of retrospectively gated MRI demonstrating tracheomalacia in a premature neonate is shown in Fig. 10.6c. This technique has been shown to quantify similar levels of airway dynamics as bronchoscopy [7].

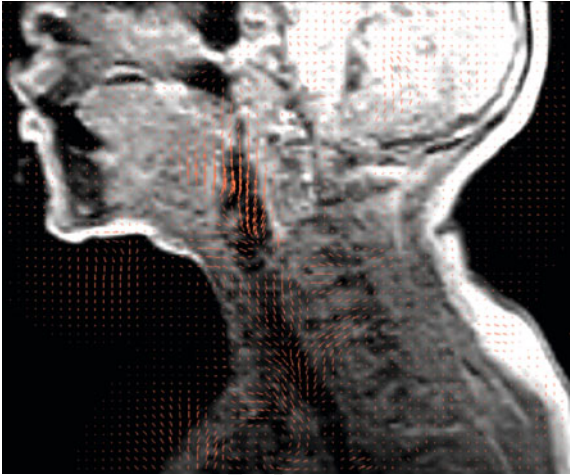
There is significant clinical value in geometric analysis of these moving airway surfaces in addition to analysis of the respiratory airflow within them. Analysis of these airway surfaces has been used in surgical planning in neonates born with tracheoesophageal defects [24] and used to predict which infants with bronchopulmonary dysplasia (respiratory disease of prematurity) will require a tracheotomy [23].

10.2.3 *Extracting Airway Motion from Cine Images*

Moving airway surfaces are extracted from images through segmentation and registration. The first image in the cine image sequence of interest must be segmented as described in Chap. 5 segmentation) and an initial airway surface generated from the segmentation. If the images are real-time cine MRI, these images may not be high enough spatial resolution to yield a good quality surface. Therefore, a high-resolution static MRI can be acquired and segmented instead and registered to the initial cine image, [9] as described below.

The goal of the registration is to produce a high-resolution, three-dimensional map of how the airway moves from each image to the next in the cine-image sequence. This can be achieved through image registration, surface registration, or a combination of both. While any non-rigid registration technique that yields suitable motion maps can be employed, an extension of the four dimensional joined, deformable motion-

Fig. 10.7 Motion vectors between 2 frames of real-time cine MRI (orange) in a pediatric patient with OSA. Between these image frames, the patient's soft palate moves down, as does the jaw. The chest expands outwards and there is some airway collapse around the larynx. Each of these motions is illustrated by large vectors in these regions



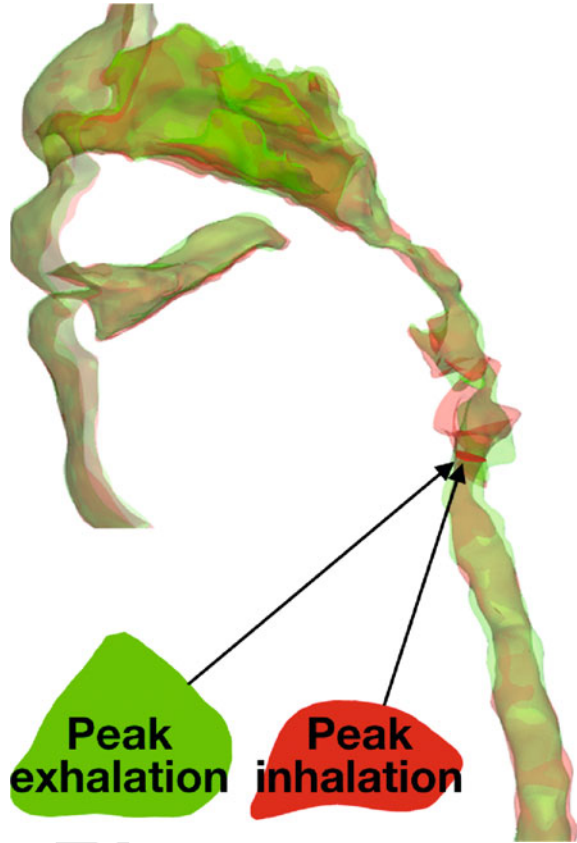
tracking algorithm originally described by Rueckert et al. [66] has been used in the examples shown in this section and has been applied to the airways previously [8, 9]. Image registration entails seeding the initial image with control points. These control points are then moved so that they are surrounded by a similar pattern of voxel intensities in the second image as they were in the first image. Adjacent control points are prevented from moving too far apart by a bending stiffness term. Surface registration requires that airway surfaces are produced based on segmentations of each image in the image sequence. Using these surfaces, registration moves control points to minimize the difference in node positions and/or surface normal vectors between the surface at one time point and the next.

The registration algorithm then minimizes the sum of the dissimilarity between consecutive images, consecutive meshes, and the bending stiffness caused by moving control points. Figure 10.7 shows airway motion vectors between one image and the next in a pediatric subject with OSA. Typical CFD time-steps for transient (i.e. temporally varying) simulations are much shorter than the period between images (<1 ms vs (O)100 ms). Therefore, the motion between each image must be interpolated to much finer temporal resolution to provide smooth motion between CFD time-steps. Figure 10.8 shows airway surfaces from a pediatric patient with sleep apnea at peak inhalation and peak exhalation. The differences between the surfaces show how the airway has moved between these timepoints.

10.2.4 Dynamic CFD Simulations

Dynamic CFD simulations require the following boundary conditions: (1) the airway surface at the initial time point; (2) the motion of this surface through the period of interest; and (3) the pressure or flow inlet and outlet boundary conditions that

Fig. 10.8 Airway surfaces at peak exhalation (green) and peak inhalation (red). The motion of the airway between these timepoints is shown where these surfaces do not overlap. A cross-sectional plane in the larynx from each timepoint is shown in the lower left



vary through the period of interest synchronously with airway motion. Flow rates throughout the breath cycle can be captured synchronously with imaging by having the subject breathe through a pneumotach. Recording these flow measurements synchronously with a trigger signal denoting each image acquisition allows alignment of airflow and motion boundary conditions, as shown in Fig. 10.9. The high frequency oscillations in the flow waveform represent snoring, which occurs faster than the temporal resolution of the MRI acquisition. However, the temporal resolution does allow changes to the airway between inhalation and exhalation to be captured.

Once these boundary conditions have been obtained, a volume mesh must be generated based on the initial surface. The transient (i.e. boundary conditions vary with time [4, 6]) CFD simulations can then be performed, as described in Chap. 7.4 (transient solutions). However, the Navier-Stokes equations must be adapted to incorporate the mesh movement. The continuity and momentum equations become

$$\frac{\partial}{\partial t} \int_{\tilde{V}} \rho \tilde{V} + \oint \rho (\mathbf{v} - \mathbf{v}_g) \cdot d\mathbf{a} = 0 \quad (10.1)$$

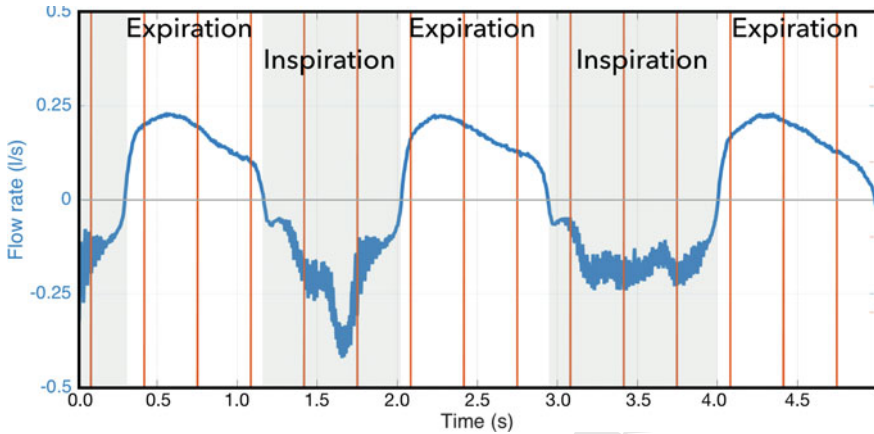


Fig. 10.9 Respiratory flow waveform (blue) and vertical red lines denoting the start time for each cine MRI acquisition (every 320 ms in this case)

and

$$\frac{\partial}{\partial t} \int_{\tilde{V}} \rho \mathbf{v} d\tilde{V} + \oint (\rho (\mathbf{v} - \mathbf{v}_g) \otimes \mathbf{v}) \cdot d\mathbf{a} = - \oint p \mathbf{I} \cdot d\mathbf{a} + \oint \mathbf{T} \cdot d\mathbf{a} \quad (10.2)$$

respectively, where t is time, \tilde{V} is the cell volume, ρ is the air density, \mathbf{v} is the airflow velocity, \mathbf{v}_g is the mesh velocity as calculated from the registration, \mathbf{a} is a vector representing the surface of each mesh cell, \mathbf{I} is the identity matrix, and \mathbf{T} is the viscous stress tensor.

Once the Navier-Stokes equations are solved for the current time-step, the mesh must be morphed to its new position. This motion may affect the quality of the mesh, which is therefore checked at each time-step. Should the mesh quality fall below the requirements for the simulation (see Chap. 6—Meshing), the current geometry should be remeshed and the pressure and flow fields interpolated onto the new mesh. Frequent remeshing can greatly extend the time taken to perform simulations, so care should be taken to produce a high-quality mesh at the initial time point. Once a mesh of suitable quality is obtained, the inlet and outlet boundary conditions are updated to the flow rates and pressures presenting the new time-step, and the Navier-Stokes equations are solved again, starting from the solution at the previous time-step. This process is repeated until the entire period of interest has been simulated.

10.2.5 Outputs from Moving Airway CFD Simulations

The prescribed motion techniques described in this section provide boundary conditions for simulations that closely follow the dynamic behavior of the in vivo airway in patients with conditions such as OSA and tracheomalacia. Velocity and local resistance fields for a patient with OSA are shown in Fig. 10.10A and B. Standard CFD output measures such as airflow velocity, pressure loss, airway resistance, and energy flux are significantly different in moving airways compared to static airways. For example, one study showed a difference in airway resistance of 76% in inhalation and 84% in exhalation between a moving airway simulation and one performed in a static airway of the same anatomy at the start of the breath [8]. In addition to providing realistic boundary conditions, moving wall CFD allows analysis of whether airway movement is due to passive (air pressure) motion, active (neuromuscular) motion, or a combination of both. For example, in OSA, muscle tone in the upper airway is an important factor in a patient’s ability to prevent airway collapse.

CFD simulations calculate the pressure forces and wall shear stress acting on the airway wall. These can be combined to show the total force acting on each face on the airway wall mesh due to the airflow, \mathbf{F}_w , as shown in equation E3, where A is the area of the face, p is the pressure force, \mathbf{n} , the normal vector to the face, and $\boldsymbol{\tau}$ the wall shear stress vector.

$$\mathbf{F}_w = A(p\mathbf{n} + \boldsymbol{\tau}) \tag{10.3}$$

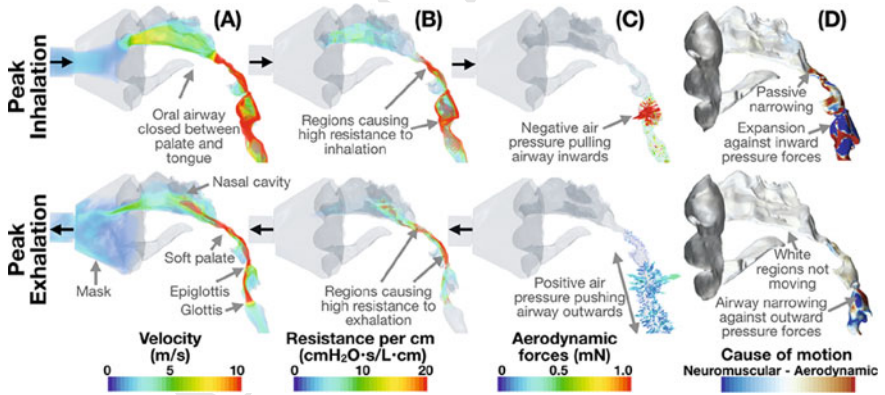


Fig. 10.10 Results from a CFD simulation in a patient with OSA with airway wall motion incorporated. **A** CFD calculations of airflow velocity showing high velocities in narrow portions of the airway. **B** Resistance per cm of airway traversed by the air-flow highlighting portions of the airway responsible for high resistance. **C** Aerodynamic force vectors (pressure plus wall shear stress). Internal pressure forces pull the airway inwards during inhalation and push outwards during exhalation. **D** The cause of airway motion determined by comparison of the direction of aerodynamic forces and the direction of motion of the airway wall. Causes of motion are due to neuromuscular control (blue), aerodynamic forces (red), or no motion (white)

Figure 10.10c shows the forces acting on the airway wall in a patient with OSA. Taking the vector dot product of this force with the prescribed airway wall velocity \mathbf{v}_w at each airway wall face allows the power transfer, P , between the airway wall and the airflow to be calculated (Eq. 10.3).

$$P = \mathbf{v}_w \cdot \mathbf{F}_w \quad (10.4)$$

This calculation determines the cause of motion between motion due to air pressure forces (passive motion) and motion caused by the airway through neuromuscular control. When the value is positive, the air pressure force is acting in the same direction as the motion of the airflow (for example, airway collapse due to sub-atmospheric air pressure in the airway), and therefore the cause of airway motion is likely to be due to airflow. However, when the airway motion and air pressure forces are in opposite directions or orthogonal to one another, the air pressure force cannot be the cause of motion, and P will be negative. Figure 10.10D shows the instantaneous power transfer between the air and the airway wall at peak inhalation and peak exhalation in a patient with OSA. This map shows regions where the airway is able to maintain patency due to neuromuscular control (blue) and where it is collapsing due to air pressure force acting on it (red).

10.2.6 Clinical Implications of Moving CFD Simulations

CFD simulations have previously revealed how airflow characteristics influence patient symptoms in patients with conditions such as stenotic tracheas, [52, 55] compressive goiters, [3, 5]. CFD simulations with realistic motion determined from cine imaging allows respiratory CFD to be applied to a wider set of airway conditions such as OSA and provides extra information that may aid in clinical decision-making. For example, surgical success rates in OSA are highly variable, as the location, cause, and degree of airway collapse varies between patients. CFD modeling may allow surgeries to be better matched to patients by calculating the regions of highest resistance (e.g. Fig. 10.10b), which indicate candidate sites for surgeries. The causes of airway collapse can also be separated into passive and neuromuscular, thereby revealing the degree of muscle tone and neuromuscular control in the patient. Finally, the airway component of the work of breathing can be calculated, allowing the energy expense of airway abnormalities to be quantified. Clinically, this can be used to develop thresholds to determine when treatments should be applied. Basing these decisions on energy expenditure rather than qualitative anatomic observations may allow treatment strategies to better match patient symptoms. Furthermore, in patients with various respiratory comorbidities, symptoms due to airway abnormalities can be separated from parenchymal respiratory issues, allowing treatments to be targeted to the regions of the respiratory symptom most responsible for symptoms

10.3 Automatic Reconstruction of the Nasal Geometry from CT Scans

Koch Walter, Lehner Matthias, Benda Odo, Ortiz Ramiro, Koch Gerda

10.3.1 Introduction

Accurate reconstruction of human nasal geometry is a critical prerequisite for realistic CFD simulations of nasal airflow. Furthermore, it is desirable that reconstruction can be performed rapidly and with minimal human intervention. Ideally, the reconstruction process can be automated completely while yielding anatomically plausible results immediately. From a clinical perspective, fast and accurate reconstruction would enable physicians as well as patients themselves to examine the nasal cavity and paranasal sinuses in an intuitive three-dimensional manner. Moreover, quickly obtained 3D models of air-filled cavities and bone provide a means for automated pathology detection, an extensive topic in its own right which will not be addressed in this chapter. From a scientific and engineering perspective, minimally time-intensive yet anatomically truthful 3D reconstructions enable the CFD specialist to focus on the investigation of nasal aerodynamics. Instead of having to expend excessive time and effort on image segmentation and 3D modelling, once a viable automated solution is available, researchers can concentrate on the *in silico* analysis of airflow and the verification of simulation results using experimental data. The latter can be obtained from sensors placed on 3D-printed models and measurements performed on patients.

In recent years, deep learning [41] algorithms have led to significant improvements in computer vision by outperforming techniques which were previously considered state-of-the-art [77]. A particular type of deep learning algorithm called a Convolutional Neural Network (CNN), which is most commonly used for image analysis (e.g. handwriting recognition [42, 43], outperforms classical approaches in many computer vision tasks. Medical image segmentation is one such task where promising results have been obtained in recent years. G. Litjens et al. [46] conducted a survey which included over 300 publications on applications of deep learning to medical image analysis published from 2012 to 2017. The survey showed that CNNs have become the prevailing deep learning algorithm in medical image analysis deduced by the number of papers published in the field which used them. In addition, image segmentation turned out to be the task they were most commonly applied to, with MR and CT images being two of the imaging modalities predominantly used. CNN architectures have, for instance, successfully been applied to segment brain tumors [30], brain lesions [31] and different brain tissues [69] in MRI, fluid abnormalities in OCT images [67], heart substructures in cardiac US [60] as well as pancreas [64], bladder [11], liver [50] and liver tumors [14] in CT images (cf. overviews of publications by topic and imaging modality in G. Litjens et al. [46]).



Based on previous work by Maninis et al. (2016) on retinal vasculature and optic disc segmentation in eye fundus images [53], we have developed CNN architectures which automate accurate segmentation of CT scans of the sinonasal cavities. The highly accurate results obtained for the thin blood vessels of the retina served as a good starting point for our work as the nasal cavity, ethmoid air cells and bones surrounding the cavities are similarly delicate (the frontal, maxillary and sphenoid sinuses are easier to segment because they constitute comparatively large, connected areas of pixels with similar intensity values).

Our CNNs work in an end-to-end fashion. This means that the CNN acts as a function which receives minimally preprocessed CT images as input and directly returns the corresponding 2D segmentations as output. The CNN assigns a class (e.g. air or not air, where 1 corresponds to air and 0 corresponds to not air) to each pixel. From the 2D segmentations, 3D models can then be generated. For instance, triangular surface meshes can be created using the Marching Cubes algorithm [49]. Note that it is also possible to implement CNNs which directly classify each voxel in a CT volume, i.e. to perform 3D segmentation [56]. We started with a 2D approach which is easier to implement and retained it because we obtained the desired results. In an initial phase, we developed separate CNNs which perform 2D segmentations of either air-filled regions or bone only, i.e. binary segmentations where white is either air or bone and black is everything else. Figure 10.11 shows two sample CT slices, the air and bone segmentation our CNNs computed for these and the 3D model generated from the segmentations of all slices of this patient’s CT volume. Note that the air surrounding the patient’s head has been removed in a post processing step and is therefore not visible in the air 3D model.

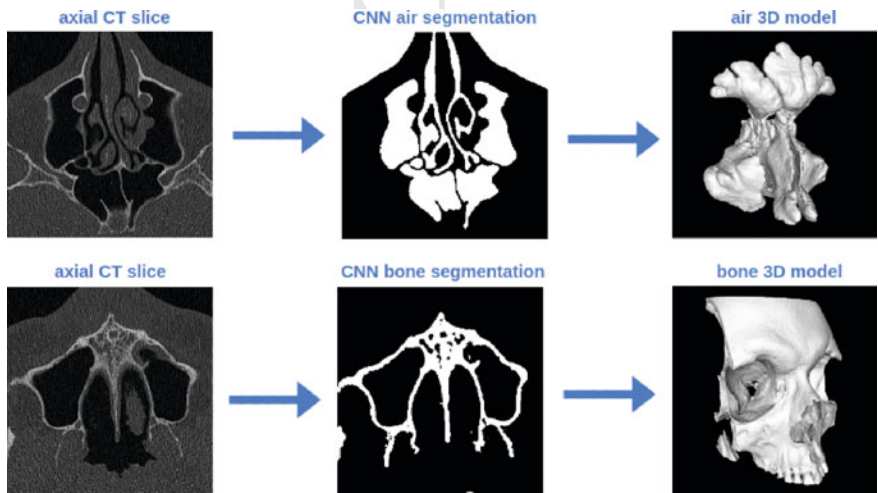


Fig. 10.11 CT slices, corresponding automatic segmentations and 3D models generated from these

10.3.2 *How Does a CNN Work and How Can a CNN Be Trained to Segment CT Images?*

This section will give an overview of what a CNN does and how it can be used for image segmentation. A CNN is a type of Artificial Neural Network (ANN) which processes images or other data represented by a grid-like topology. Digital images can be represented as matrices of real-valued pixel intensity values. In the case of grayscale CT images, each pixel has a single intensity value which represents the brightness of the pixel (shade of gray). We want the CNN to learn to infer whether a given pixel should be classified as either air or not air (or as either bone or not bone, i.e. as one class or the other). A CNN can achieve this goal by using several layers which perform different mathematical operations. These operations allow a CNN to extract information about the neighbourhood of a given pixel to decide if the pixel should belong to one class or the other.

Our CNN architecture consists of multiple Convolution Layers, each followed by a Nonlinearity (ReLU Layer) and a Max Pooling Layer. The most important layer, the one which gives the CNN its name, performs a (discrete) convolution and is hence called a Convolution Layer. It performs an element-wise multiplication of pixel intensity values in a neighbourhood of each pixel of the input image with the scalar elements of a so called filter matrix, followed by addition of the re-sulting terms (linear combination) [18]. This is how image filters (kernels) work. The result is a new image (matrix) called a feature map. Applying a convolution matrix to an image filters it to extract certain features. Note that in mathematics, the described operation is called a cross-correlation, but in the context of image processing the term convolution is used. A CNN's architecture is loosely inspired by the workings of neurons in the human visual system as the neighbourhood around a given pixel can be viewed as a receptive field and the connectivity pattern of the neurons of a CNN bears resemblance to visual cortex organization [26].

Typically, a nonlinear function (most often a so-called rectified linear unit, ReLU) is applied to the output of the convolution. This makes the output a non-linear function of the inputs. By applying many convolutions to an input image, a CNN can extract different features from an image. Each convolution results in a different feature map. By combining the information from many such feature maps, a CNN can then assign a certain class to each pixel of an input image.

Furthermore, convolutions can also be applied to the feature maps themselves to obtain additional feature maps. By using multiple successive Convolutional Layers, more abstract features can be extracted (e.g. an initial layer may provide information about simple geometric features like edges, a deeper layer may involve more abstract features like the general shape of a given cavity, i.e. one obtains a feature hierarchy). Using several layers in this way makes a neural network deeper, hence the term deep learning. In our CNNs, a volume of feature maps is linearly combined to obtain a single prediction matrix containing real values. The values in this matrix can then be mapped to probabilities in (0, 1) by applying a so called activation function (e.g. a sigmoid function). In a final step, a threshold is applied to this probability matrix.



This sets each value greater than or equal to 0.5 to 1 (air) and each value less than 0.5 to 0 (not air), thereby obtaining a binary segmentation.

The elements of a convolution matrix are called weights. In traditional image processing, the programmer specifies the weights of a convolution matrix to achieve a desired effect (e.g. sharpening of an image). Using a CNN, the task of assigning a class to each pixel in an image can be formulated as a mathematical optimization problem where a cost function is minimized. Weights can be initialized randomly and are improved over time rather than being manually specified by the programmer at the outset. The CNN is fed with pairs of CT images and manual segmentations as inputs. Each input helps the CNN learn better values for the weights, where better means that the cost becomes smaller, which itself means that the CNN outputs a segmentation which is more similar to the manual segmentation it is provided with (which serves as an example for what the desired output looks like). This way the CNN becomes progressively better at segmenting images by learning from examples. Figure 10.12 shows an illustration of the basic architecture of our CNN (for 2 Convolutional Layers, we use up to 4, but some of our best CNNs only use a single layer).

A CNN is trained with so-called supervised learning. This means that a CNN is provided with training data in the form of input-output pairs (CT images paired with segmentations which are manually created by a human expert) where the provided outputs tell the CNN what the desired output is supposed to look like for new inputs. This allows the CNN to learn from the provided examples. Once fully trained, the CNN can segment CT images it has not seen before. Segmentation and 3D model generation for an entire CT volume of e.g. 1000 slices is then reduced to 3 min instead of several days. The so-called labelled data consists of CT images of different patients (DICOM files obtained from partnering clinics) and manual segmentations created for them. We use 256×256 px partial images (our CT images have a resolution of 512×512 px, we use only a region of interest) of axial slices. The Hounsfield unit range is mapped to $[0, 1]$ as a pre-processing step. Rotated and scaled versions of these axial CT slices can also be included in the dataset to create more data artificially (data augmentation). Segmentations for a subset of patients were created manually, this took several days. The manual segmentations were then inspected visually and checked for accuracy and anatomical plausibility by a practicing ENT (Ear-Nose-Throat) surgeon. Three datasets (training, validation and test set) were created from these images, where each dataset consists of both, CT images and their corresponding manual segmentations. First, the training set was used to train many CNNs with different so-called hyperparameters (described in the following paragraphs). Second, the validation set was used to select the top-performing CNN from these. Third, since this selection process can lead to overfitting on the validation set, the performance was confirmed by assessing the CNN's performance on the test set. As a heuristic, training, validation and test set often constitute 60%, 20% and 20% of the entire, randomized dataset.

In each iteration a single CT image is passed through the CNN to generate segmentations (forward pass). The cost, for instance the cross entropy between the probability matrix and the human segmentation, averaged over all images used, is then propagated back to update the weights (backward pass, back propagation of



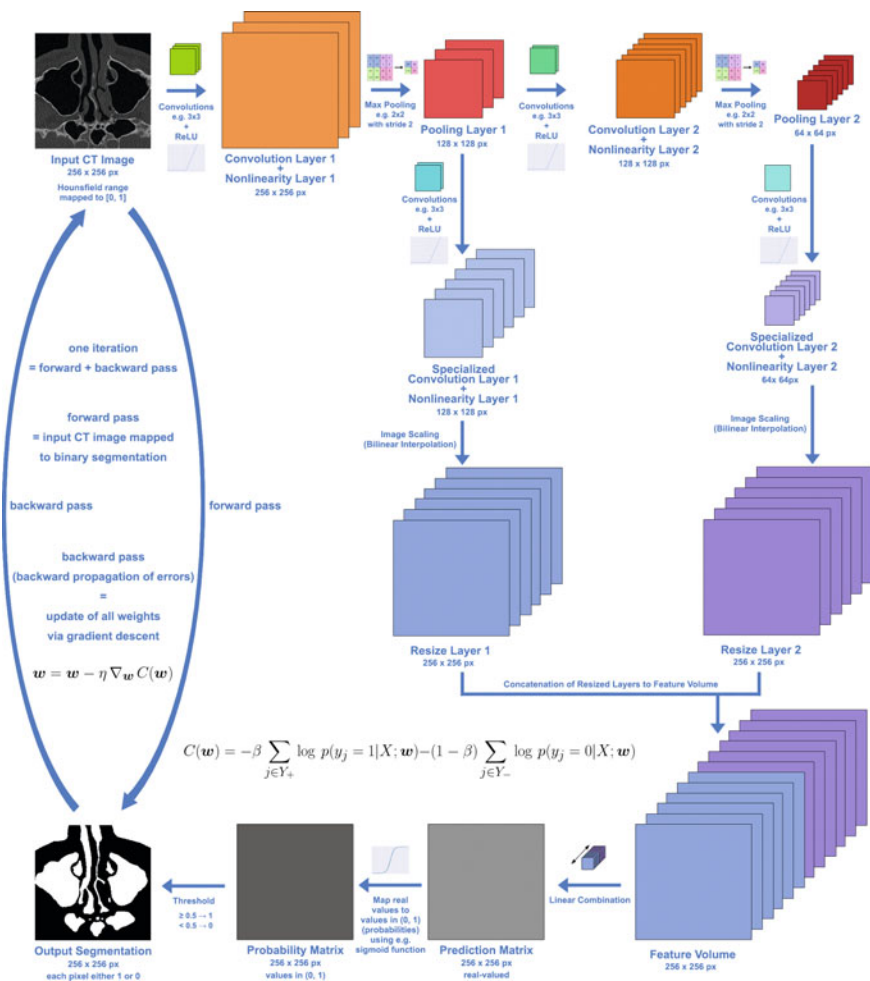


Fig. 10.12 Basic architecture of our binary segmentation CNNs (for either air or bone segmentation)

errors). This process is called stochastic gradient descent (if one training image is used each iteration and gradient descent is taken to perform updates of the weights). A step size (learning rate) is set to specify how much the weights should be adjusted within each iteration. Performing this process iteratively improves the weights and hence the obtained segmentations. The learning process is stopped once certain metrics are met, for instance once the accuracy (percentage of pixels which are the same in both CNN and human segmentation) is high enough. CNNs with different hyperparameters (number of layers, number and size of filter matrices, step sizes etc.) are trained and the top performing ones selected using the validation and test sets. We obtained good results for a constant step size of 0.01 using up to 10 filter matrices

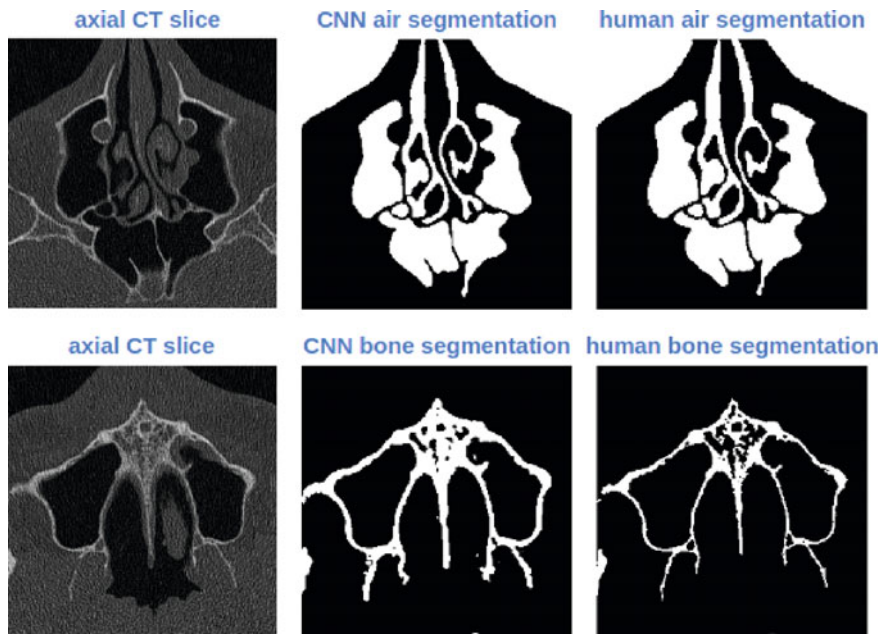


Fig. 10.13 CNN air and bone segmentation results compared to segmentations generated by a human

of size 3×3 or 5×5 for each Convolution Layer, 1 to 4 layers in total, mean cross entropy as the cost function and either Adam or Momentum as optimizer to perform stochastic gradient descent [32, 65]. The CNNs were trained for about 1000 to 5000 iterations on an NVIDIA GTX 1080 GPU and stopped once requirements for metrics such as accuracy, overlap (Jaccard index) and similar number of connected components were met.

Figure 10.13 shows a comparison of automated and human segmentations obtained for 2 sample CT images. Our top performing CNNs achieve an accuracy of 99–96% for air segmentation and an accuracy of 95–96% for bone segmentation. The latter is more difficult because bones and surrounding tissue often have very similar intensity values and are often hard to distinguish even for human experts due to the noise in the CT images. Figure 10.14 illustrates how the segmentation outputs of a CNN improve over time.

In a second phase, motivated by the good results for binary segmentations, we developed a CNN which, instead of predicting for a single pixel whether it belongs to a single class or not, predicts whether the pixel belongs to one of multiple classes. This is achieved by performing a different linear combination of the feature map volume for each class, which results in a vector of class probabilities for each pixel. The predicted class is then given by the largest element of this vector. We trained CNNs for either 11 classes (left/right frontal/sphenoid/maxillary sinus, nasal cavity, oral cavity, air outside, bone and tissues) or 9 classes (left/right frontal/sphenoid

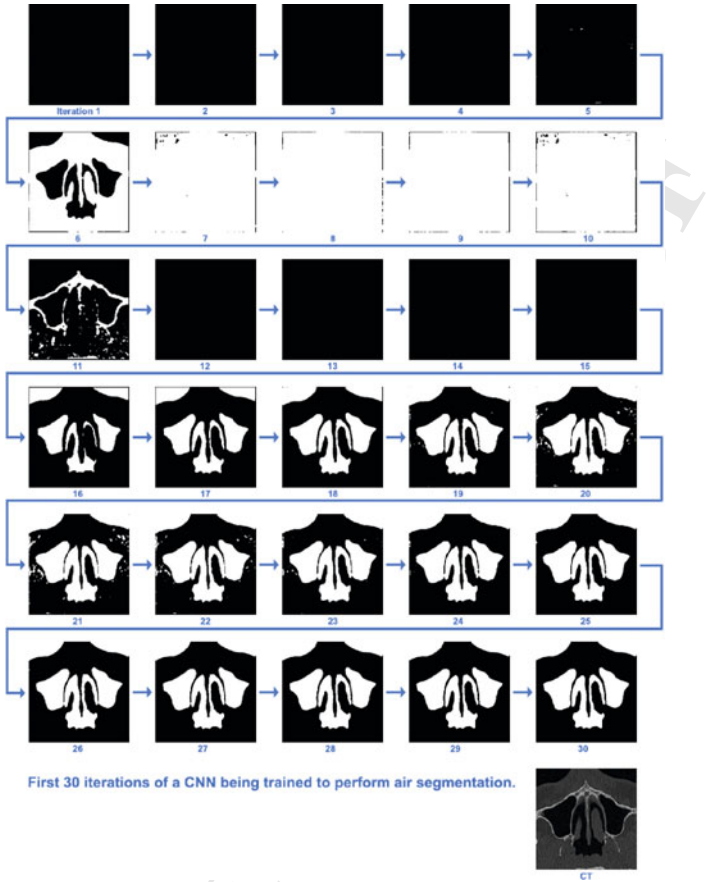


Fig. 10.14 CNN segmentation results for a single CT image during the first 30 iterations of training (CT image is taken from validation set; to update weights during training, a different CT image is used in each iteration)

sinus, left and right maxillary sinuses combined, nasal and oral cavity combined, air outside, bone and tissues). The maxillary sinuses are not adjacent to each other as they are located on opposite sides of the head. They can therefore be combined into a single layer and are easily separated later once the 3D model has been generated. Oral and nasal cavities need not necessarily be separate segments if one does not want to distinguish between the two. In general, a lower number of classes is easier to process accurately for the CNN. Figure 10.15 shows preliminary results obtained for 2 sample CT slices by a CNN trained to distinguish 11 different classes. By learning a distinct class for each type of cavity and tissue, the CNN also learns to distinguish air from bone more accurately and there is no overlap between any of the segments.

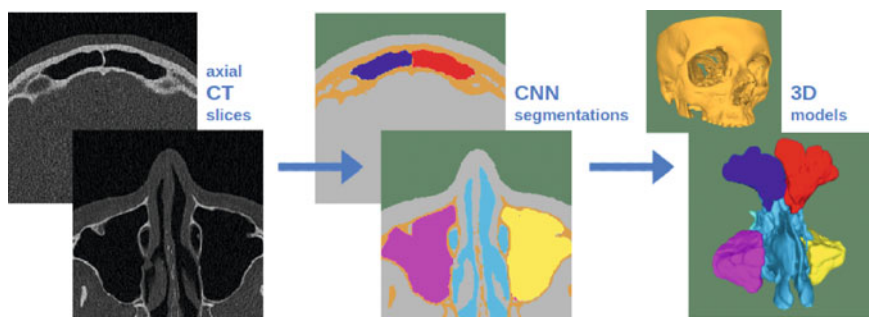


Fig. 10.15 Axial CT slices, the multi-class segmentations computed by a CNN, and the 3D models generated from these

As some classes are found in more CT images than others, form components of different size than others and make up different percentages of the total number of pixels, class balancing techniques may be required (e.g. focal loss [44] or an adequate sampling strategy [10, 63]). At the moment, the CNNs we have trained do not learn each class similarly well. Hence we are currently in the process of optimizing our results for multi-class segmentation by experimenting with different approaches to handle imbalanced classes. Once our approach has been refined, accurate 3D models of bone, tissues and individual cavities shall be obtained for new patients within minutes. Currently, this research work is partly funded by the COIN/IraSME project Rhinodiagnost, Morphological and Functional Precision Diagnostics for the Nose [45].

References

1. B. Asgharian, W. Hofmann, R. Bergmann, Particle deposition in a multiple-path model of the human lung. *Aerosol Sci. Technol.* **34**(4), 332–339 (2001)
2. S. Ashaat, A.M. Al-Jumaily, Reducing upper airway collapse at lower continuous positive airway titration pressure. *J. Biomech.* **49**(16), 3915–3922 (2016)
3. A. Bates, R. Cetto, D. Doorly, R. Schroter, N. Tolley, A. Comerford, The effects of curvature and constriction on airflow and energy loss in pathological tracheas. *Respir. Physiol. Neurobiol.* **234**, 69–78 (2016)
4. A. Bates, A. Comerford, R. Cetto, D. Doorly, R. Schroter, N. Tolley, Computational fluid dynamics benchmark dataset of airflow in tracheas. *Data Brief* **10**, 101–107 (2017)
5. A. Bates, A. Comerford, R. Cetto, R. Schroter, N. Tolley, D. Doorly, Power loss mechanisms in pathological tracheas. *J. Biomech.* **49**(11), 2187–2192 (2016)
6. A.J. Bates, D.J. Doorly, R. Cetto, H. Calmet, A. Gambaruto, N. Tolley, G. Houzeaux, R. Schroter, Dynamics of airflow in a short inhalation. *J. R. Soc. Interface* **12**(102), 20140880 (2015)
7. A.J. Bates, N.S. Higano, E.B. Hysinger, R.J. Fleck, A.D. Hahn, S.B. Fain, P.S. Kingma, J.C. Woods, Quantitative assessment of regional dynamic airway collapse in neonates via retrospectively respiratory-gated 1h ultrashort echo time mri. *J. Magn. Reson. Imaging* **49**(3), 659–667 (2019)

8. A.J. Bates, A. Schuh, G. Amine-Eddine, K. McConnell, W. Loew, R.J. Fleck, J.C. Woods, C.L. Dumoulin, R.S. Amin, Assessing the relationship between movement and airflow in the upper airway using computational fluid dynamics with motion determined from magnetic resonance imaging. *Clin. Biomech.* **66**, 88–96 (2017)
9. A.J. Bates, A. Schuh, K. McConnell, B.M. Williams, J.M. Lanier, M.M. Willmering, J.C. Woods, R.J. Fleck, C.L. Dumoulin, R.S. Amin, A novel method to generate dynamic boundary conditions for airway cfd by mapping upper airway movement with non-rigid registration of dynamic and static mri. *Int. J. Numer. Methods Biomed. Eng.* **34**(12), e3144 (2018)
10. G.E. Batista, R.C. Prati, M.C. Monard, A study of the behavior of several methods for balancing machine learning training data. *ACM SIGKDD Explor. Newsl.* **6**(1), 20–29 (2004)
11. K.H. Cha, L.M. Hadjiiski, R.K. Samala, H.-P. Chan, R.H. Cohan, E.M. Caoili, C. Paramagul, A. Alva, A.Z. Weizer, Bladder cancer segmentation in ct for treatment response assessment: application of deep-learning convolution neural network—a pilot study. *Tomography* **2**(4), 421 (2016)
12. S. Cheng, S. Gandevia, M. Green, R. Sinkus, L. Bilston, Viscoelastic properties of the tongue and soft palate using mr elastography. *J. Biomechan.* **44**(3), 450–454 (2011)
13. J.I. Choi, C.S. Kim, Mathematical analysis of particle deposition in human lungs: An improved single path transport model. *Inhal. Toxicol.* **19**, 925–939 (2007)
14. P.F. Christ, M.E.A. Elshaer, F. Ettlinger, S. Tatavarty, M. Bickel, P. Bilic, M. Rempfler, M. Armbruster, F. Hofmann, M. DÄÄŽAnastasi et al., Automatic liver and lesion segmentation in ct using cascaded fully convolutional neural networks and 3d conditional random fields, in *International Conference on Medical Image Computing and Computer-Assisted Intervention* (Springer, Berlin, 2016), pp. 415–423
15. A. Comerford, C. Forster, W.A. Wall, Structured tree impedance outflow boundary conditions for 3d lung simulations. *J. Biomechan. Eng.* **132**, 10 (2010)
16. J. Dong, Y. Shang, K. Inthavong, H.-K. Chan, J. Tu, Numerical comparison of nasal aerosol administration systems for efficient nose-to-brain drug delivery. *Pharm. Res.* **35**(1), 5 (2018)
17. G. Dournes, D. Grodzki, J. Macey, P.-O. Girodet, M. Fayon, J.-F. Chateil, M. Montaudon, P. Berger, F. Laurent (2015) Quiet submillimeter mr imaging of the lung is feasible with a petra sequence at 1.5 t. *Radiology* **276**(1), 258–265
18. V. Dumoulin, F. Visin, A guide to convolution arithmetic for deep learning. [arXiv:1603.07285](https://arxiv.org/abs/1603.07285) (2016)
19. Y. Feng, C. Kleinstreuer, Analysis of non-spherical particle transport in complex internal shear flows. *Phys. Fluids* **25**(9), 091904 (2013)
20. Y. Feng, Z. Xu, A. Haghnegahdar, Computational fluid-particle dynamics modeling for unconventional inhaled aerosols in human respiratory systems. *Aerosols-Science and Case Studies* (2016)
21. Y. Feng, J. Zhao, C. Kleinstreuer, Q. Wang, J. Wang, D.H. Wu, J. Lin, An in silico inter-subject variability study of extra-thoracic morphology effects on inhaled particle transport and deposition. *J. Aerosol Sci.* **123**, 185–207 (2018)
22. A. Haghnegahdar, Y. Feng, X. Chen, J. Lin, Computational analysis of deposition and translocation of inhaled nicotine and acrolein in the human body with e-cigarette puffing topographies. *Aerosol Sci. Technol.* **52**(5), 483–493 (2018)
23. N. Higano, A. Bates, E. Hysinger, I. St. Onge, R. Fleck, P. Kingma, J. Woods, Dynamic tracheal collapse and correlation to later tracheostomy in neonates with bronchopulmonary dysplasia via quantitative ultrashort echo-time mri, in *C16. Clinical Studies in Bronchopulmonary Dysplasia* (American Thoracic Society, New York, 2019), pp. A4264–A4264
24. N.S. Higano, A.J. Bates, J.A. Tkach, R.J. Fleck, F.Y. Lim, J.C. Woods, P.S. Kingma, Pre- and post-operative visualization of neonatal esophageal atresia/tracheoesophageal fistula via magnetic resonance imaging. *J. Pediatr. Surg. Case Rep.* **29**, 5–8 (2018)
25. N.S. Higano, A.D. Hahn, J.A. Tkach, X. Cao, L.L. Walkup, R.P. Thomen, S.L. Merhar, P.S. Kingma, S.B. Fain, J.C. Woods, Retrospective respiratory self-gating and removal of bulk motion in pulmonary ute mri of neonates and adults. *Magn. Reson. Med.* **77**(3), 1284–1295 (2017)



26. D.H. Hubel, T.N. Wiesel, Receptive fields and functional architecture of monkey striate cortex. *J. Physiol.* **195**(1), 215–243 (1968)
27. K. Inthavong, Z. Tian, J. Tu, W. Yang, C. Xue, Optimising nasal spray parameters for efficient drug delivery using computational fluid dynamics. *Comput. Biol. Med.* **38**(6), 713–726 (2008)
28. T. Janke, P. Koullapis, S. Kassinos, K. Bauer, Piv measurements of the siminhale benchmark case. *Eur. J. Pharm. Sci.* **133**, 183–189 (2019)
29. K.M. Johnson, S.B. Fain, M.L. Schiebler, S. Nagle, Optimized 3d ultrashort echo time pulmonary mri. *Magn. Reson. Med.* **70**(5), 1241–1250 (2013)
30. K. Kamnitsas, E. Ferrante, S. Parisot, C. Ledig, A.V. Nori, A. Criminisi, D. Rueckert, B. Glocker, Deepmedic for brain tumor segmentation, in *International workshop on Brainlesion: Glioma, multiple sclerosis, stroke and traumatic brain injuries* (Springer, Berlin, 2016), pp. 138–149
31. K. Kamnitsas, C. Ledig, V.F. Newcombe, J.P. Simpson, A.D. Kane, D.K. Menon, D. Rueckert, B. Glocker, Efficient multi-scale 3d cnn with fully connected crf for accurate brain lesion segmentation. *Med. Image Anal.* **36**, 61–78 (2017)
32. D.P. Kingma, J. Ba, Adam: A method for stochastic optimization. [arXiv:1412.6980](https://arxiv.org/abs/1412.6980) (2014)
33. L. Koblinger, W. Hofmann, Analysis of human lung morphometric data for stochastic aerosol deposition calculations. *Phys. Med. Biol.* **30**(6), 541–556 (1985)
34. L. Koblinger, W. Hofmann, Monte carlo modeling of aerosol deposition in human lungd. part i: Simulation of particle transport in a stochastic lung structure. *J. Aerosol Sci.* **21**(5), 661–674 (1990)
35. A.V. Kolanjiyil, C. Kleinstreuer, Nanoparticle mass transfer from lung airways to systemic regions—part i: Whole-lung aerosol dynamics. *J. Biomechan. Eng.* **135**(12), 11 (2013)
36. A.V. Kolanjiyil, C. Kleinstreuer, Nanoparticle mass transfer from lung airways to systemic regions—part ii: Multi-compartmental modeling. *J. Biomech. Eng.* **135**, 12 (2013)
37. A.V. Kolanjiyil, C. Kleinstreuer, Computationally efficient analysis of particle transport and deposition in a human whole-airway model. part i: theory and model validation. *Comput. Biol. Med.* **76**, 193–204 (2016)
38. A.V. Kolanjiyil, C. Kleinstreuer, Computational analysis of aerosol-dynamics in a human whole-lung airway model. *J. Aerosol Sci.* **114**, 301–316 (2017)
39. A.V. Kolanjiyil, C. Kleinstreuer, R.T. Sadikot, Computationally efficient analysis of particle transport and deposition in a human whole-lung-airway model. part ii: Dry powder inhaler application. *Comput. Biol. Med.* **2017**, 247–253 (2017)
40. P. Koullapis, P. Hofemeier, J. Sznitman, S. Kassinos, An efficient computational fluid-particle dynamics method to predict deposition in a simplified approximation of the deep lung. *Eur. J. Pharm. Sci.* **113**, 132–144 (2018)
41. Y. LeCun, Y. Bengio, G. Hinton, Deep learning. *Nature* **521**(7553), 436–444 (2015)
42. Y. LeCun, B. Boser, J.S. Denker, D. Henderson, R.E. Howard, W. Hubbard, L.D. Jackel, Backpropagation applied to handwritten zip code recognition. *Neural Comput.* **1**(4), 541–551 (1989)
43. Y. LeCun, L. Bottou, Y. Bengio, P. Haffner et al., Gradient-based learning applied to document recognition. *Proc. IEEE* **86**(11), 2278–2324 (1998)
44. T.-Y. Lin, P. Goyal, R. Girshick, K. He, P. Dollár, Focal loss for dense object detection, in *Proceedings of the IEEE International Conference on Computer Vision*, pp. 2980–2988 (2017)
45. A. Lintermann, J. Göbbert, K. Vogt, W. Koch, A. Hetzel, Rhinodiagnost-morphological and functional precision diagnostics of nasal cavities. *InSiDE, Innov. Supercomput. Dtsch.* **15**(2), 106–109 (2017)
46. G. Litjens, T. Kooi, B.E. Bejnordi, A.A.A. Setio, F. Ciompi, M. Ghafoorian, J.A. Van Der Laak, B. Van Ginneken, C.I. Sánchez, A survey on deep learning in medical image analysis. *Med. Image Anal.* **42**, 60–88 (2017)
47. P.W. Longest, G. Tian, R. Delvadia, M. Hindle, Development of a stochastic individual path (sip) model for predicting the deposition of pharmaceutical aerosols: Effects of turbulence, polydisperse aerosol size, and evaluation of multiple lung lobes. *Aerosol Sci. Technol.* **46**(12), 1271–1285 (2012)



48. P.W. Longest, G. Tian, N. Khajeh-Hosseini-Dalasm, M. Hindle, Validating whole-airway cfd predictions of dpi aerosol deposition at multiple flow rates. *J. Aerosol Med. Pulm. Drug Deliv.* **29**(6), 461–481 (2016)
49. W.E. Lorensen, H.E. Cline, Marching cubes: A high resolution 3d surface construction algorithm, in *ACM siggraph computer graphics*, vol. 21 (ACM, New York, 1987), pp. 163–169
50. F. Lu, F. Wu, P. Hu, Z. Peng, D. Kong, Automatic 3d liver location and segmentation via convolutional neural network and graph cut. *Int. J. Comput. Assist. Radiol. Surg.* **12**(2), 171–182 (2017)
51. B. Ma, K.R. Lutchen, An anatomically based hybrid computational model of the human lung and its application to low frequency oscillatory mechanics. *Ann. Biomed. Eng.* **34**(11), 1691–1704 (2006)
52. M. Malvè, A. Pérez del Palomar, S. Chandra, J. López-Villalobos, A. Mena, E. Finol, A. Ginel, M. Doblaré, Fsi analysis of a healthy and a stenotic human trachea under impedance-based boundary conditions. *J. Biomech. Eng.* **133**, 2 (2011)
53. K.-K. Maninis, J. Pont-Tuset, P. Arbeláez, L. Van Gool, Deep retinal image understanding, in *International conference on medical image computing and computer-assisted intervention* (Springer, Berlin, 2016), pp. 140–148
54. T.B. Martonen, Analytical model of hygroscopic particle behavior in human airways. *Bull. Math. Biol.* **44**(3), 425–442 (1982)
55. M. Mihaescu, E. Gutmark, R. Elluru, J.P. Willging, Large eddy simulation of the flow in a pediatric airway with subglottic stenosis, in *47th AIAA Aerospace Sciences Meeting including The New Horizons Forum and Aerospace Exposition*, p. 775 (2009)
56. F. Milletari, N. Navab, S.-A. Ahmadi, V-net: Fully convolutional neural networks for volumetric medical image segmentation. *2016 Fourth International Conference on 3D Vision (3DV)*, pp. 565–571 (2016)
57. M. Monjezi, R. Dastanpour, M.S. Saidi, A.R. SPishevari, Prediction of particle deposition in the respiratory track using 3d–1d modeling. *Sci. Iran.* **19**(6), 1479–1486 (2012)
58. A.I. Pack, Dynamic upper airway imaging during awake respiration in normal subjects and patients with sleep disordered breathing. *Am. Rev. Respir. Dis.* **148**, 1385–1400
59. A. Pandal-Blanco, R. Barrio-Perotti, R. Agujetas-Ortiz, A. Fernandez-Tena, Implementation of a specific boundary condition for a simplified symmetric single path cfd lung model with openfoam. *Biomech. Model. Mechanobiol.* **18**, 1759–1771 (2019)
60. C. Payer, D. Štern, H. Bischof, M. Urschler, Multi-label whole heart segmentation using cnns and anatomical label configurations, in *International Workshop on Statistical Atlases and Computational Models of the Heart* (Springer, Berlin, 2017), pp. 190–198
61. M.S. Pearce, J.A. Salotti, M.P. Little, K. McHugh, C. Lee, K.P. Kim, N.L. Howe, C.M. Ronckers, P. Rajaraman, A.W. Craft et al., Radiation exposure from ct scans in childhood and subsequent risk of leukaemia and brain tumours: a retrospective cohort study. *Lancet* **380**(9840), 499–505 (2012)
62. J. Pirnar, L. Dolenc-Grošelj, I. Fajdiga, I. Žun, Computational fluid-structure interaction simulation of airflow in the human upper airway. *J. Biomech.* **48**(13), 3685–3691 (2015)
63. F. Provost, Machine learning from imbalanced data sets 101, in *Proceedings of the AAAI 2000 workshop on imbalanced data sets*, vol. 68 (AAAI Press, Palo Alto, CA, 2000), pp. 1–3
64. H.R. Roth, L. Lu, N. Lay, A.P. Harrison, A. Farag, A. Sohn, R.M. Summers, Spatial aggregation of holistically-nested convolutional neural networks for automated pancreas localization and segmentation. *Med. Image Anal.* **45**, 94–107 (2018)
65. S. Ruder, An overview of gradient descent optimization algorithms. [arXiv:1609.04747](https://arxiv.org/abs/1609.04747) (2016)
66. D. Rueckert, L.I. Sonoda, C. Hayes, D.L. Hill, M.O. Leach, D.J. Hawkes, Nonrigid registration using free-form deformations: Application to breast mr images. *IEEE Trans. Med. Imaging* **18**(8), 712–721 (1999)
67. T. Schlegl, S.M. Waldstein, W.-D. Vogl, U. Schmidt-Erfurth, G. Langs, Predicting semantic descriptions from medical images with convolutional neural networks, in *International Conference on Information Processing in Medical Imaging* (Springer, Berlin, 2015), pp. 437–448



68. R.J. Schwab, W.B. Gefter, A.I. Pack, E.A. Hoffman, Dynamic imaging of the upper airway during respiration in normal subjects. *J. Appl. Physiol.* **74**(4), 1504–1514 (1993)
69. M. Shakeri, S. Tsogkas, E. Ferrante, S. Lippe, S. Kadoury, N. Paragios, I. Kokkinos, Sub-cortical brain structure segmentation using f-cnn's, in *2016 IEEE 13th International Symposium on Biomedical Imaging (ISBI)* (IEEE, Prague, 2016), pp. 269–272
70. W.-C. Su, Y.S. Cheng, Estimation of carbon nanotubes deposition in a human respiratory tract replica. *J. Aerosol Sci.* **79**, 72–85 (2015)
71. W.-C. Su, B.K. Ku, P. Kulkarni, Y.S. Cheng, Deposition of graphene nanomaterial aerosols in human upper airways. *J. Occup. Environ. Hyg.* **13**(1), 48–59 (2016)
72. B. Suki, R.H. Habib, A.C. Jackson, Wave propagation, input impedance, and wall mechanics of the calf trachea from 16 to 1,600 hz. *Am. Physiol. Soc.* **75**(6), 2755–2766 (1993)
73. D.B. Taulbee, C.P. Yu, A theory of aerosol deposition in the human respiratory tract. *J. Appl. Physiol.* **38**(1), 77–85 (1975)
74. M.H. Tawhai, A.J. Pullan, P.J. Hunter, Generation of an anatomically based three-dimensional model of the conducting airways. *Ann. Biomed. Eng.* **28**, 793–802 (2000)
75. A. Tena, J. Fernandez, E. Alvarez, P. Casan, D.K. Walters, Design of a numerical model of lung by means of a special boundary condition in the truncated branches. *Int. J. Numer. Meth. Biomed. Eng.* **33**(6), 1–9 (2016)
76. I.E. Vignon-Clementel, C.A. Figueroa, K.E. Jansen, C.A. Taylor, Outflow boundary conditions for three-dimensional finite element modeling of blood flow and pressure in arteries. *Comput. Methods Appl. Mech. Eng.* **195**, 3776–3796 (2006)
77. A. Voulodimos, N. Doulamis, A. Doulamis, E. Protopapadakis, Deep learning for computer vision: A brief review. *Comput. Intell. Neurosci.* **2018**, 7068349 (2018)
78. D.K. Walters, W.H. Luke, Computational fluid dynamics simulations of particle deposition in large-scale, multigenerational lung models. *J. Biomech. Eng.* **133**(1), 011003 (2011)
79. Y. Wang, J. Wang, Y. Liu, S. Yu, X. Sun, S. Li, S. Shen, W. Zhao, Fluid-structure interaction modeling of upper airways before and after nasal surgery for obstructive sleep apnea. *Int. J. Numer. Methods Biomed. Eng.* **28**(5), 528–546 (2012)
80. E. Weibel, *Morphometry of the human lung* (Academic Press, New York, 1963)
81. Z. Zhang, C. Kleinstreuer, C.S. Kim, Airflow and nanoparticle deposition in a 16-generation tracheobronchial airway model. *Ann. Biomed. Eng.* **36**(19), 2095–2110 (2008)
82. M. Zhao, T. Barber, P. Cistulli, K. Sutherland, G. Rosengarten, Predicting the treatment response of oral appliances for obstructive sleep apnea using computational fluid dynamics and fluid-structure interaction simulations, in *ASME 2013 International Mechanical Engineering Congress and Exposition*, American Society of Mechanical Engineers Digital Collection, New York (2013)
83. M. Zhao, T. Barber, P.A. Cistulli, K. Sutherland, G. Rosengarten, Simulation of upper airway occlusion without and with mandibular advancement in obstructive sleep apnea using fluid-structure interaction. *J. Biomech.* **46**(15), 2586–2592 (2013)
84. J.H. Zhu, H.P. Lee, K.M. Lim, S.J. Lee, L.S.L. Teo, D.Y. Wang, Passive movement of human soft palate during respiration: A simulation of 3d fluid/structure interaction. *J. Biomech.* **45**(11), 1992–2000 (2012)



MARKED PROOF

Please correct and return this set

Please use the proof correction marks shown below for all alterations and corrections. If you wish to return your proof by fax you should ensure that all amendments are written clearly in dark ink and are made well within the page margins.

<i>Instruction to printer</i>	<i>Textual mark</i>	<i>Marginal mark</i>
Leave unchanged	... under matter to remain	Ⓟ
Insert in text the matter indicated in the margin	⧵	New matter followed by ⧵ or ⧵ [Ⓢ]
Delete	/ through single character, rule or underline or ⎯ through all characters to be deleted	⧻ or ⧻ [Ⓢ]
Substitute character or substitute part of one or more word(s)	/ through letter or ⎯ through characters	new character / or new characters /
Change to italics	— under matter to be changed	↵
Change to capitals	≡ under matter to be changed	≡
Change to small capitals	≡ under matter to be changed	≡
Change to bold type	~ under matter to be changed	~
Change to bold italic	≈ under matter to be changed	≈
Change to lower case	Encircle matter to be changed	≡
Change italic to upright type	(As above)	⧻
Change bold to non-bold type	(As above)	⧻
Insert 'superior' character	/ through character or ⧵ where required	Y or Y under character e.g. Y or Y
Insert 'inferior' character	(As above)	⧵ over character e.g. ⧵
Insert full stop	(As above)	⊙
Insert comma	(As above)	,
Insert single quotation marks	(As above)	Y or Y and/or Y or Y
Insert double quotation marks	(As above)	Y or Y and/or Y or Y
Insert hyphen	(As above)	⎯
Start new paragraph	┐	┐
No new paragraph	┐	┐
Transpose	┐	┐
Close up	linking ○ characters	○
Insert or substitute space between characters or words	/ through character or ⧵ where required	Y
Reduce space between characters or words		↑